J. Fluid Mech. (2023), *vol*. 954, A16, doi:10.1017/jfm.2022.1003

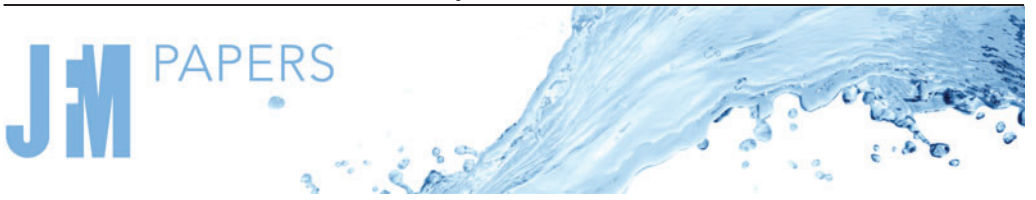

Bubble re-acceleration behaviours in compressible Rayleigh–Taylor instability with isothermal stratification

Cheng-Quan Fu[1], **Zhiye Zhao**[1,†], **Pei Wang**[2], **Nan-Sheng Liu**[1], **Zhen-Hua Wan**[1] **and Xi-Yun Lu**[1]

[1]Department of Modern Mechanics, University of Science and Technology of China, Hefei, Anhui 230026, PR China

[2]Institute of Applied Physics and Computational Mathematics, Beijing 100094, PR China

(Received 18 July 2022; revised 23 October 2022; accepted 30 November 2022)

The highly nonlinear evolution of the single-mode stratified compressible Rayleigh–Taylor instability (RTI) is investigated via direct numerical simulation over a range of Atwood numbers ($A_T = 0.1$–0.9) and Mach numbers ($Ma = 0.1$–0.7) for characterising the isothermal background stratification. After the potential stage, it is found that the bubble is accelerated to a velocity which is well above the saturation value predicted in the potential flow model. Unlike the bubble re-acceleration behaviour in quasi-incompressible RTI with uniform background density, the characteristics in the stratified compressible RTI are driven by not only vorticity accumulation inside the bubble but also flow compressibility resulting from the stratification. Specifically, in the case of strong stratification and high A_T, the flow compressibility dominates the bubble re-acceleration characters. To model the effect of flow compressibility, we propose a novel model to reliably describe the bubble re-acceleration behaviours in the stratified compressible RTI, via introducing the dilatation into the classical model that takes into account only vorticity accumulation.

Key words: buoyancy-driven instability

1. Introduction

Rayleigh–Taylor instability (RTI) occurs in the interface when a light fluid is accelerated against a heavy fluid (Rayleigh 1882; Taylor 1950). It has been widely encountered as an important role in supernovae ignition fronts (Burrows 2000; Swisher *et al.* 2015), inertial confinement fusion (Zhang *et al.* 2020) and various topics in geophysics (Wilcock & Whitehead 1991; Houseman & Molnar 1997; Zhou 2017). In these problems, the

† Email address for correspondence: zzy12@ustc.edu.cn

background or initial state is stratified and the Reynolds number is large, resulting in flow compressibility over a wide range of length and time scales (Wieland *et al.* 2019; Luo *et al.* 2020; Fu *et al.* 2022). However, the effects of flow compressibility on the stratified compressible RTI evolution, especially at the highly nonlinear stage, are still unclear and thus of great interest for further detailed studies.

Since great advancement has been achieved for the RTI evolution from linear to nonlinear saturation stages (Layzer 1955; Goncharov 2002), increasingly more research interests are being focused on the subsequent highly nonlinear evolution of the instability after the nonlinear saturation stage. Previous experiments (Wilkinson & Jacobs 2007) and numerical simulations (Betti & Sanz 2006; Ramaprabhu *et al.* 2006; Banerjee *et al.* 2011; Ramaprabhu *et al.* 2012; Yan *et al.* 2016; Hu *et al.* 2019; Bian *et al.* 2020) have shown that the elegant potential model (Goncharov 2002) analytically predicting the bubble saturation velocity becomes inapplicable when RTI achieves the highly nonlinear evolution. In ablative RTI, Betti & Sanz (2006) revealed that attributed to vorticity accumulation inside the bubble resulting from the vorticity convection off the ablation front, the bubble is re-accelerated to velocities well above the saturation value. They have successfully described the bubble re-acceleration (RA) behaviours by introducing the vorticity to improve the saturation velocity model. It is also found that a similar phenomenon occurs in classical RTI at low Atwood numbers, where the secondary Kelvin–Helmholtz instabilities are responsible for vorticity generation leading to bubble RA (Ramaprabhu *et al.* 2006, 2012; Hu *et al.* 2019), and the Betti–Sanz model is proven again to reliably describe the RA behaviours. Bian *et al.* (2020) conducted a systematic analysis of the effects of perturbation Reynolds number Re_p and Atwood number A_T on the highly nonlinear evolution of RTI using fully compressible simulations with uniform background density. Their main conclusions are that the bubble re-accelerates to speeds above the saturation velocity when Re_p is sufficiently large, and increasing A_T with Re_p fixed suppresses the bubble front development resulting from that the longer travel distances for vortices to enter the bubble tip region at higher A_T lead to the dissipative attenuation of vortices for a fixed Re_p.

Isothermal stratification has complicated effects on the compressible RTI flows, although its influence on highly nonlinear bubble evolution has not been well studied. Specifically, isothermal stratification can either suppress or enhance the growth of RTI at the nonlinear saturation stage, depending upon the value of A_T at the interface (Reckinger, Livescu & Vasilyev 2012, 2016; Luo *et al.* 2020; Fu *et al.* 2022). As the hydrostatic and thermal equilibriums are initialised consistently in numerical simulations, the commensurate density stratification suppresses the bubble growth for small A_T by reducing the buoyancy driving the bubble (Reckinger *et al.* 2012, 2016). Luo *et al.* (2020) revealed that the enhancement of bubble growth for high A_T is related to the expansion–compression effect (i.e. flow compressibility effect). Fu *et al.* (2022) further proposed a modified buoyancy-drag model to interpret the enhancement of bubble growth at the nonlinear saturation stage. For high A_T, density stratification reduces the drag on the bubble greatly whereas the buoyancy is relatively slightly, which makes the rising bubble compress the heavy fluid ahead of the fronts and enhance the bubble growth (Fu *et al.* 2022). It is worth noting that flow compressibility becomes dominating in compressible RTI of strong stratification and high A_T due to the compression of heavy fluid exerted by the rising bubble. Furthermore, flow compressibility is critical to the RTI evolution, such as converting the internal energy into the kinetic energy of RTI (Zhao *et al.* 2020*b*; Luo & Wang 2021; Zhao, Betti & Aluie 2022) and resulting the asymmetries in the RTI growth (Wieland *et al.* 2019).

Motivated by the aforementioned findings, the goal of this work is to find the effects of flow compressibility on the highly nonlinear evolution of the stratified compressible RTI, with special interest directed to answer the following questions. Can similar bubble RA behaviours occur in a stratified compressible RTI? Of special interest, how will flow compressibility coupled with vorticity accumulation set in the bubble RA? Towards this goal, direct numerical simulation (DNS) of two-dimensional (2-D) single-mode stratified compressible RTI is performed to examine the highly nonlinear bubble growth behaviour via increasing the stratification strength at different A_T values. The present focus on initial stratification strength is intended to reveal the effects of flow compressibility on RTI evolution.

2. Numerical simulations

2.1. *Governing equations*

According to the previous studies (Wieland *et al.* 2019; Fu *et al.* 2022), the perturbation wave length (λ^*), initial temperature (T_I^*), density (ρ_I^*) and the isothermal speed of sound ($U_I^* \equiv \sqrt{p_I^*/\rho_I^*}$) at the interface are chosen as the characteristic scales. The initial pressure p_I^* can be obtained from the ideal gas equation of state, i.e. $p_I^* = \rho_I^* \mathcal{R}^* T_I^*/[(W_h^* + W_l^*)/2]$, where W_h^* and W_l^* represent the molar masses of the heavy and light fluids, respectively, and $\mathcal{R}^*$ is the universal gas constant. The dimensional physical quantities at the initial interface are denoted by the subscript 'I' and the superscript '*'. The dimensionless governing equations read as

$$\frac{\partial \rho}{\partial t} + \frac{\partial (\rho u_i)}{\partial x_i} = 0, \tag{2.1}$$

$$\frac{\partial (\rho u_i)}{\partial t} + \frac{\partial (\rho u_i u_j)}{\partial x_j} = -\frac{\partial p}{\partial x_i} + \frac{1}{Re}\frac{\partial \sigma_{ij}}{\partial x_j} - Ma^2 \rho \delta_{i2}, \tag{2.2}$$

$$\frac{\partial (\rho e)}{\partial t} + \frac{\partial [(\rho e + p) u_i]}{\partial x_i} = \frac{1}{Re}\frac{\partial}{\partial x_i}(\sigma_{ij} u_j + q_i^T + q_i^Y) - Ma^2 \rho u_2, \tag{2.3}$$

$$\frac{\partial (\rho Y_h)}{\partial t} + \frac{\partial (\rho Y_h u_i)}{\partial x_i} = \frac{1}{ReSc}\frac{\partial}{\partial x_i}\left(\rho D \frac{\partial Y_h}{\partial x_i}\right), \tag{2.4}$$

where ρ is the fluid density, u_i is the velocity component in the x_i direction, i.e. $(u_1, u_2) = (u, v)$ with $(x_1, x_2) = (x, y)$, $e = C_v T + u_i u_i/2$ denotes the specific total energy with C_v being the specific heats at constant volume, $Y_h = \rho_h/\rho$ is the species mass fraction of heavy fluid and $Y_l = 1 - Y_h$ is the species mass fraction of light fluid, the pressure p is calculated by the dimensionless ideal gas equation of state $p = \rho T/W$ and the molar mass of fluid W is calculated by $1/W = Y_h/W_h + Y_l/W_l$ and δ_{ij} is the Kronecker symbol. The shear stress tensor is obtained as

$$\sigma_{ij} = \mu\left(\frac{\partial u_i}{\partial x_j} + \frac{\partial u_j}{\partial x_i}\right) - \frac{2\mu\delta_{ij}}{3}\frac{\partial u_k}{\partial x_k}, \tag{2.5}$$

where the viscosity coefficient $\mu = (T)^{3/2}(1 + c)/(T + c)$ is computed by the Sutherland law with $c = 124/T_r$ and T_r being the reference temperature. The heat flux for the thermal

(q_i^T) and interspecies mass (q_i^Y) diffusions (Li *et al.* 2019), are defined as

$$q_i^T = \frac{\gamma\kappa}{(\gamma-1)Pr}\frac{\partial T}{\partial x_i}, \quad q_i^Y = \sum_{m=h,l}\frac{\rho D C_{pm} T}{Sc}\frac{\partial Y_m}{\partial x_i}, \tag{2.6a,b}$$

where κ is the heat conduction coefficient, γ is the ratio of specific heat, D is the diffusion coefficient and C_{pm} is the constant-pressure specific heat with $m = h, l$ denoting the heavy and light fluids. The fluid properties are defined as linear combinations of the individual species' properties weighted by the mass fractions, for example, $C_v = \sum_{m=h,l} C_{vm} Y_m$.

The dimensionless parameters in the governing equations (2.1)–(2.4) are the Mach number Ma, the Reynolds number Re, the Schmidt number Sc and the Prandtl number Pr, defined by

$$Ma = \sqrt{\frac{g^*\lambda^*}{p_I^*/\rho_I^*}}, \quad Re = \frac{\rho_I^* U_I^* \lambda^*}{\mu_I^*}, \quad Sc = \frac{\mu_I^*/\rho_I^*}{D_I^*}, \quad Pr = C_{pI}^*\frac{\mu_I^*}{\kappa_I^*}, \tag{2.7a–d}$$

respectively. Here, the Mach number characterises the strength of the isothermal background stratification (Livescu 2004; Reckinger *et al.* 2012, 2016).

2.2. *Initialisation and numerical methods*

Owing to the RTI initiated with a hydrostatic equilibrium ($u_i = 0$), the momentum equation (2.2) can be integrated analytically with the ideal gas equation of state and the isothermal assumption ($T = 1$) (Reckinger *et al.* 2012, 2016; Hu *et al.* 2019) to give

$$\rho_{h,l}^H = (1 \pm A_T)\exp[-Ma^2(1 \pm A_T)y], \tag{2.8}$$

$$p_{h,l}^H = \exp[-Ma^2(1 \pm A_T)y], \tag{2.9}$$

where $A_T = (W_h^* - W_l^*)/(W_h^* + W_l^*)$ is the Atwood number. To smooth the interface density jump, the error function is introduced (Reckinger *et al.* 2012; Hu *et al.* 2019).

A single-mode perturbation, $I(x) = a_0\cos(2\pi x)$, where $a_0 = 0.02\lambda$ is the perturbation amplitude (Luo *et al.* 2020), is introduced at the initially flat interface positioned at $y = 0$ to launch the RTI. In the present study, we set a range of Mach numbers ($Ma = 0.1 \sim 0.7$) and Atwood numbers ($A_T = 0.1 \sim 0.9$) to examine the bubble RA behaviours with various stratification strengths and density ratios. As pointed by Bian *et al.* (2020), the perturbation Reynolds number ($Re_p \equiv \rho_I^*\lambda^*\sqrt{A_T/(1+A_T)g^*\lambda^*}/\mu_I^*$) has a significant influence on the bubble RA behaviours. For $Re_p \geqslant 1000$, the bubble re-accelerates transiently but then decelerates at small $A_T \leqslant 0.25$. Nevertheless, for $Re_p \geqslant 6000$, the bubble re-accelerates robustly at late times when A_T is small. To this end, the perturbation Reynolds number Re_p is chosen as 1500 and 10 000, high enough for the RTI flow to evolve into the RA stage and to study the influence of Re_p. Other parameters in the governing equations (2.1)–(2.4) are fixed as $Pr = 0.72$, $Sc = 1$ and $\gamma = 1.4$. The computational domain sizes are set as $L_x \times L_y = [0, 1] \times [-10, 10]$ for $Ma = 0.1 \sim 0.5$, $L_x \times L_y = [0, 1] \times [-10, 8]$ for $Ma = 0.6$ and $L_x \times L_y = [0, 1] \times [-10, 6]$ for $Ma = 0.7$. In addition, the bubble height h_b refers to the distance from $y = 0$ to the bubble tip location y_b where the average mass fraction value $\bar{Y}_h$ along the x-axis equals 99 % (Wieland *et al.* 2019), and the bubble velocity V_b is computed from the derivative of the bubble height to time ($V_b = \mathrm{d}h_b/\mathrm{d}t$). To compare the nonlinear bubble behaviours in the cases of different parameter settings, the bubble velocity and time in the following discussions are rescaled to ensure that the

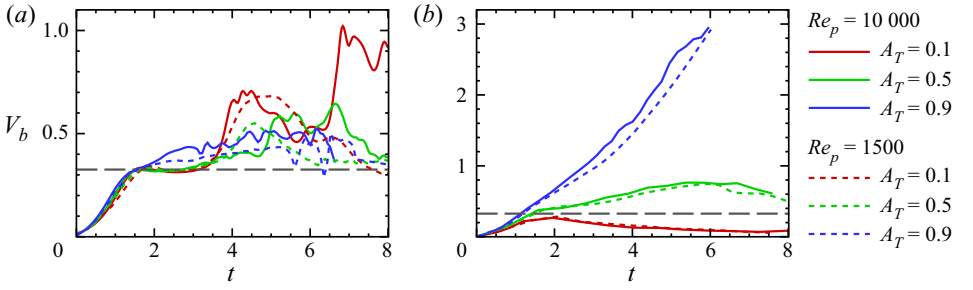

Figure 1. The bubble velocity V_b versus time for (*a*) weak ($Ma = 0.1$) and (*b*) strong ($Ma = 0.7$) stratification strengths. The solid and dashed lines in each panel represent the bubble velocities with $Re_p = 10\,000$ and $Re_p = 1500$, respectively. The horizontal black long dashed line in each panel represents the bubble saturated velocity V_t predicted in potential flow models.

bubbles have the same scaled velocity when entering the nonlinear stage at the same scaled time. To this end, we follow the recent work (Bian *et al.* 2020; Luo *et al.* 2020) using a time scale $\sqrt{\lambda/(A_T g)}$ that is obtained by the RTI linear growth rate $\gamma = \sqrt{A_T g k}$ (Rayleigh 1882; Taylor 1950) to characterise the time, for which the coefficient $\sqrt{2\pi}$ introduced by the wavenumber $k = 2\pi/\lambda$ is left out. As for the scaling of the bubble velocity, the saturated velocity $V_t = \sqrt{A_T g \lambda/[3\pi(1 + A_T)]}$ is used neutrally as the characteristic velocity while leaving out the coefficient $\sqrt{1/(3\pi)}$, as done by Bian *et al.* (2020) and Fu *et al.* (2022).

The high-fidelity DNS has been performed to solve the governing equations (2.1)–(2.4) in the present study. Specifically, the convection and diffusion terms are discretised by the seven-order WENO scheme and eight-order central difference scheme, respectively, and the third-order Runge–Kutta scheme is employed for the time integration (Zhao, Liu & Lu 2020*a*; Zhao *et al.* 2020*b*; Fu *et al.* 2022). Periodic boundary conditions are applied along the x-direction, and the variables, i.e. ρ, u_i, e and Y_h, are fixed at their initialised values at the y-direction boundaries (Reckinger *et al.* 2012; Hu *et al.* 2019; Hu, Zhang & Tian 2020; Luo *et al.* 2020). To meet the requirement for the mesh Grashoff numbers ($Gr_\Delta = 2A_T g \Delta^3/\nu_I^2$) below 1 (Cabot & Cook 2006; Bian *et al.* 2020; Luo & Wang 2021), the uniform square mesh sizes Δ for $Re_p = 1500$ and 10 000 are set as 0.005 and 0.00125, respectively.

In addition, we have carefully examined the physical model and numerical approach used in this study and have verified that the calculated results are reliable in our previous work on compressible Rayleigh–Taylor flows (Zhao *et al.* 2020*a*,*b*, 2021; Fu *et al.* 2022).

3. Bubble RA behaviours

To investigate the bubble RA behaviours in stratified compressible RTI, the bubble velocity V_b is plotted in figure 1 at different A_T and Re_p for weak ($Ma = 0.1$) and strong ($Ma = 0.7$) stratification strengths. At early time, V_b increases exponentially for all cases and reaches the nonlinearly saturated value V_t predicted by potential flow models at $t \approx 1.5$. After that, the bubble undergoes RA so that V_b is well above V_t except for the cases with $Ma = 0.7$ and $A_T = 0.1$. However, the effects of A_T on the RA behaviour are quite different for $Ma = 0.1$ and 0.7. For weak stratification ($Ma = 0.1$), increasing the A_T from 0.1 to 0.9 while keeping Re_p fixed at 1500 or 10 000 reduces the maximum value of V_b (see figure 1*a*), which is consistent with the effect of A_T in unstratified RTI where the RA results from vorticity accumulation inside the bubble (Bian *et al.* 2020). The effect of A_T

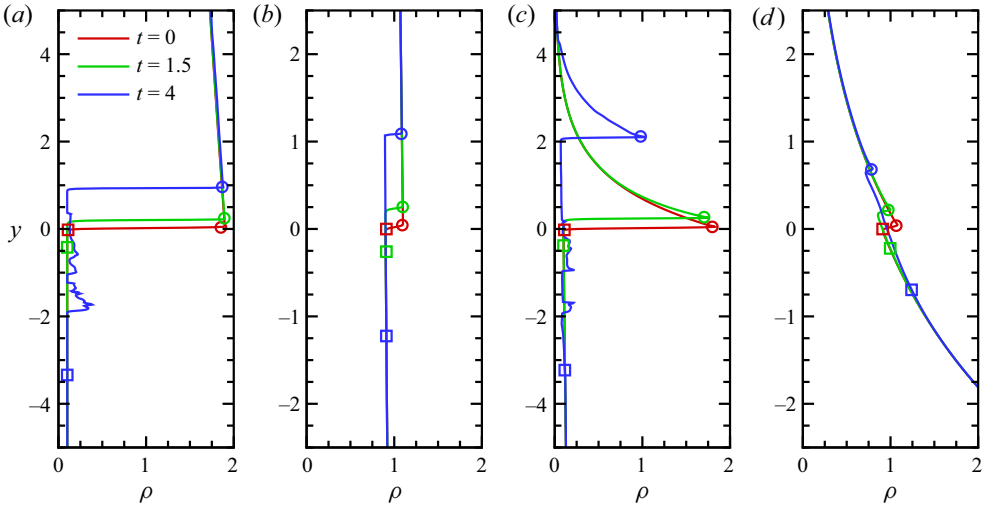

Figure 2. The density profiles along the vertical lines across the bubble tip ($x = 0$) with $Re_p = 10\,000$ for (*a*) $Ma = 0.1, A_T = 0.9$, (*b*) $Ma = 0.1, A_T = 0.1$, (*c*) $Ma = 0.7, A_T = 0.9$ and (*d*) $Ma = 0.7, A_T = 0.1$. The circle marked on the density profile denotes the vertical position of the bubble tip and the square represents the position of the spike tip at each moment.

is attributed to the fact that the sites of vortex generation around the sinking spike drift further away from the bubble tip at higher A_T, corresponding to a longer travel distance so that vortices obtain an attenuated dissipation before entering the bubble tip region for a fixed Re_p (Bian *et al.* 2020). Unlike the effect of A_T on the bubble RA behaviours at $Ma = 0.1$, for strong stratification ($Ma = 0.7$), it is clearly seen in figure 1(*b*) that the bubble accelerates more robustly at higher A_T and decreasing A_T from 0.9 to 0.1 suppresses the bubble front development. In particular, at low A_T (e.g. $A_T = 0.1$), V_b starts to decrease after reaching the saturated value.

These interesting behaviours of the bubble at high Ma can be explained by examining the balance between the buoyancy and drag forces via the modified buoyancy-drag model (BDM) proposed in our previous study (Fu *et al.* 2022). Note that, for the unstratified RTI, balance is realised for the buoyancy and drag forces resulting in a saturated bubble velocity at the potential stage, for example, at the critical moment $t \approx 1.5$ when $h_b \approx 0.2\lambda$ (Wei & Livescu 2012). Therefore, the variations of the buoyancy and drag forces estimated by the modified BDM with respect to their unstratified counterparts are used to account for the bubble velocity characteristics. As indicated in figure 2, as the bubble height grows at high $Ma = 0.7$, the density difference at the bubble tip decreases corresponding to a decrease in the buoyancy driving the bubble compared with the unstratified counterparts; this situation also happens to the drag force due to the decrease of the heavy fluid density in front of the bubble. For example, in the high-Ma stratified RTI of $A_T = 0.9$ at $t \approx 1.5$, the modified BDM estimates a decrease extent of 7.47 % in the buoyancy and of 10.52 % in the drag compared with its unstratified counterpart; in the case of $A_T = 0.1$, the decrease extent is estimated as 7.55 % for the buoyancy and 6.27 % for the drag. Accordingly, the growing bubble obtains a late-time robust acceleration at high $A_T = 0.9$ whereas there is a deceleration at low $A_T = 0.1$. Thus, decreasing A_T from 0.9 to 0.1 suppresses the bubble front development, as observed in figure 1(*b*).

Figure 1 also presents a striking dependence of bubble RA behaviours on Re_p at $Ma = 0.1$ and 0.7. For weak stratification ($Ma = 0.1$), there are two different trends at

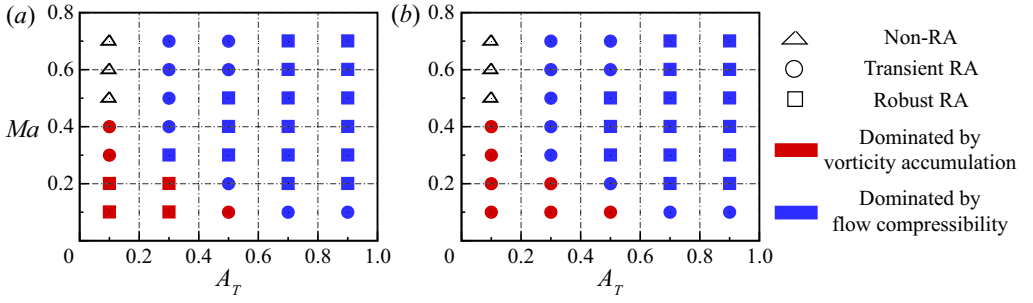

Figure 3. Phase diagram of Ma–A_T illustrating the bubble RA with (*a*) $Re_p = 10\,000$ and (*b*) $Re_p = 1500$. Red and blue symbols indicate that the bubble RA mechanism is dominated by vorticity accumulation and flow compressibility, respectively.

$A_T = 0.1$ for the V_b development when $Re_p = 1500$ and 10 000. Specifically, for $A_T = 0.1$ in figure 1(*a*), V_b of $Re_p = 1500$ starts to decay after accelerating to twice the saturated velocity, whereas V_b of $Re_p = 10\,000$ undergoes a further RA at $t \approx 6$. In addition, figure 1(*a*) shows a clear trend of more intense fluctuations in V_b for $Re = 10\,000$ with respect to $Re_p = 1500$ at a fixed A_T. This significant dependence of RA behaviours on Re_p also appears in unstratified RTI, and Bian *et al.* (2020) attributes it to less vorticity dissipation at higher Re_p which leads to more vortices accumulating inside the bubble tip resulting in higher vorticity and, in turn, V_b fluctuating in time. In contrast to the great V_b dependence on Re_p at $Ma = 0.1$, the V_b values are almost the same in the cases of strong stratification for $Re_p = 1500$ and 10 000 (see figure 1*b*) at a fixed A_T, indicating a weak influence of Re_p on V_b.

To further elucidate the RA behaviours in stratified compressible RTI, the late-time behaviour of the bubble is classified into three phases in figure 3 according to Bian *et al.* (2020): robust RA, transient RA and non-RA. A robust RA phase denotes that the bubble re-accelerates robustly at late times (e.g. $Ma = 0.1$, $A_T = 0.1$ with $Re_p = 10\,000$ and $Ma = 0.7$, $A_T = 0.9$ with $Re_p = 1500$ or 10 000); in the transient RA phase, a bubble re-accelerates transiently but then decelerates (e.g. $Ma = 0.1$, $A_T = 0.1$ with $Re_p = 1500$ and $Ma = 0.7$, $A_T = 0.5$ with $Re_p = 1500$ or 10 000); in the non-RA phase, bubble velocity starts to decay before reaching the saturated value (e.g. $Ma = 0.7$, $A_T = 0.1$ with $Re_p = 1500$ or 10 000). Figure 3(*a*) summarises the following findings in a phase diagram in the (Ma, A_T) space with $Re_p = 10\,000$. (1) For $Ma = 0.1$, the late-time bubble is in the robust RA phase at small $A_T \leqslant 0.3$ and becomes the transient RA phase as A_T is increased to a larger value. (2) When $Ma = 0.2$, the late-time bubble is in the robust RA phase at large $A_T \geqslant 0.7$. (3) For $0.3 \leqslant Ma \leqslant 0.4$, increasing A_T at a constant Re_p leads to a phase change for the late-time bubble from transient RA to robust RA. (4) For higher $Ma \geqslant 0.5$, the late-time bubble at low $A = 0.1$ is in the non-RA phase. Increasing A_T changes the bubble phase from non-RA to transient RA and finally to robust RA. For comparison, figure 3(*b*) presents the Ma-A_T phase diagram illustrating the bubble RA with $Re_p = 1500$. In contrast to the cases of $Re_p = 10\,000$, the bubble phase of $Re_p = 1500$ changes from robust RA to transient RA at small Ma and A_T, but unaltered at high $Ma \geqslant 0.4$. The effects of A_T and Re_p on the bubble RA behaviour at strong stratification differs from those at weak stratification, indicating that a novel mechanism coupling vorticity accumulation and flow compressibility sets in the later-time bubble RA for the stratified compressible RTI at high Ma.

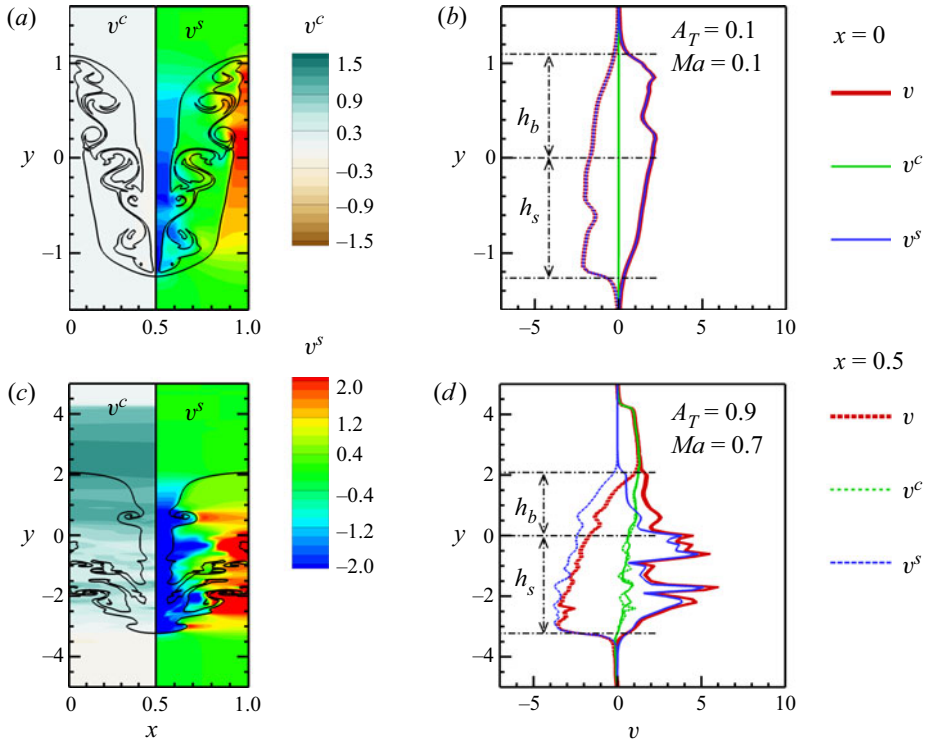

Figure 4. (*a*,*c*) Contour plots of compressive (v^c, left half) and the solenoidal (v^s, right half) components of vertical velocity v and (*b*,*d*) profiles of v, v^c, and v^s along the vertical lines across the bubble ($x = 0$, denoted by the solid lines) and spike ($x = 0.5$, denoted by dashed lines) tips with $Re_p = 10\,000$ for (*a*,*b*) $A_T = 0.1$, $Ma = 0.1$ and (*c*,*d*) $A_T = 0.9$, $Ma = 0.7$ at $t = 4$ when the bubble is in the robust RA phase. The dark lines in panels (*a*,*c*) represent the heavy/light fluid interface where $Y_h = 0.5$.

4. Bubble RA model

The bubble RA in quasi-incompressible RTI is driven by vorticity accumulation inside the bubble based on some studies (Ramaprabhu *et al.* 2006, 2012; Hu *et al.* 2019; Bian *et al.* 2020). For stratified compressible RTI, our most recent work shows that drag reduction on the bubble caused by stratification leads to the compression of the heavy fluid in front of the bubble, namely, the increased flow compressibility becomes more important to enhance the bubble growth (Fu *et al.* 2022). Here, to clarify the role that flow compressibility plays in the RA mechanism, we employ the velocity Helmholtz decomposition (Wang *et al.* 2013), i.e.

$$u_i = u_i^s + u_i^c, \tag{4.1}$$

where $(u_1^s, u_2^s) = (u^s, v^s)$ and $(u_1^c, u_2^c) = (u^c, v^c)$ are the solenoidal and compressive (irrotational) components, respectively. The clear flow physics are indicated by the contour plots of v^c and v^s with $Re_p = 10\,000$ for the case $Ma = 0.1$, $A_T = 0.1$ (figure 4*a*) and $Ma = 0.7$, $A_T = 0.9$ (figure 4*c*) at $t = 4$ when the bubble is in the robust RA phase. For weak stratification of $A_T = 0.1$, it is clearly seen in figure 4(*a*) that abundant vortices generated at the spike's interface penetrate into the bubble tip and v^s is dominant to v inside the bubble (see figure 4*b*). The vertical compressive velocity v^c in figure 4(*a*) is almost zero over the whole field, indicating that the effects of flow compressibility can

be ignored for the case with $Ma = 0.1$ and $A_T = 0.1$. However, for strong stratification of $A_T = 0.9$, v^c is significant across the bubble tip (see figure 4*d*) caused by the compression of the rising bubble on the heavy fluid in its front (Fu *et al.* 2022). It is also noted in figure 4(*c*) that v^s near the bubble tip is negligible compared with v^c, because it is difficult at high A_T for the vortices generated at the spike interface to be convected into the bubble front (Bian *et al.* 2020). In addition, figure 4(*c*) presents that v^c near the bubble tip is almost uniform along the horizontal direction.

The analysis shows that both vorticity accumulation and flow compressibility work as the mechanisms driving the bubble RA in stratified compressible RTI. In order to determine which of these two mechanisms is dominant, based on the fact that the bubble velocity ($V_b = \mathrm{d}h_b/\mathrm{d}t$) is equal to the vertical velocity of fluid at the bubble tip (v_b) (Goncharov 2002), V_b can be decomposed into V_b^s and V_b^c by setting $V_b^s = v_b^s$ and $V_b^c = v_b^c$. Here, v_b^s and v_b^c denote the solenoidal and compressive components of v_b, which are related to the vorticity and the dilatation, respectively. Furthermore, the values of $\langle V_b^s - V_b^s|_{t_s}\rangle$ and $\langle V_b^c - V_b^c|_{t_s}\rangle$ correspond to the contributions of vorticity accumulation and flow compressibility at the bubble RA stage, respectively. Here, $\langle\cdot\rangle$ denotes the time average from the moment (t_s) when the bubble velocity reaches the saturation value of the unstratified RTI to the end of simulation, $V_b^s|_{t_s}$ and $V_b^c|_{t_s}$ denote the values of V_b^s and V_b^c at time t_s, respectively. It is clearly shown in figure 3 that flow compressibility dominates the bubble RA behaviour in the cases of strong stratification and high A_T whereas vorticity accumulation dominates at small Ma and small A_T. Therefore, the A_T effect and Re_p effect at strong stratification are different from those at weak stratification (see figure 1).

Next, we attempt to propose a model to describe the bubble RA behaviours in stratified compressible RTI, quantifying the effects of vorticity accumulation and flow compressibility. As different mechanisms, V_b^s and V_b^c need to be modelled separately. Bian *et al.* (2020) modified the RA model (Betti & Sanz 2006) by adding an efficiency factor $\eta = 0.45$ to the vorticity term to account for the attenuation of vortices as they travel through the bubble tip region and predict well the bubble RA behaviours driven by vorticity accumulation. In that, V_b^s in stratified compressible RTI can also be modelled as

$$V_b^\omega = \sqrt{\frac{g(1-r_d)}{C_d k} + \eta r_d \frac{\omega_0^2}{4k^2}}. \tag{4.2}$$

Here, $C_d = 3$ for two dimensions, $\omega_0 = \int_V \rho|\omega|\,\mathrm{d}V / \int_V \rho\,\mathrm{d}V$, $\omega = \partial v/\partial x - \partial u/\partial y$ and V is the volume inside the bubble from the bubble front to a vertical distance of $2/k$ below (k is the wavenumber). Here $r_d = \rho_l'/\rho_h'$ is the density ratio where ρ_h' is the maximum density at the bubble vertex and ρ_l' is average density in the volume V (Betti & Sanz 2006). It is shown in figure 5(*a*,*d*,*g*) that the model V_b^ω agrees well with V_b^s evaluated from DNS. Note that the V_b^ω model can also predict the suppression effects at small A_T caused by the stratification on the bubble growth (e.g. the case at $A_T = 0.1$ and $Ma = 0.7$).

For V_b^c caused by flow compressibility, the dilatation θ (i.e. divergence of velocity) has been introduced naturally to the model. According to the Helmholtz decomposition, $\theta = \partial u_i^c/\partial x_i$. By employing Green's formula, integrating θ yields

$$\iint_S \theta\,\mathrm{d}S = \oint_{\partial S} u^c\,\mathrm{d}y - v^c\,\mathrm{d}x. \tag{4.3}$$

Here, S is the integral region above the bubble tip ($y_b = h_b$) where the heavy fluid is compressed by the bubble, i.e. $S = [0, L_x] \times [y_b, y_{+\infty}]$, where $y_{+\infty}$ is referred to as any

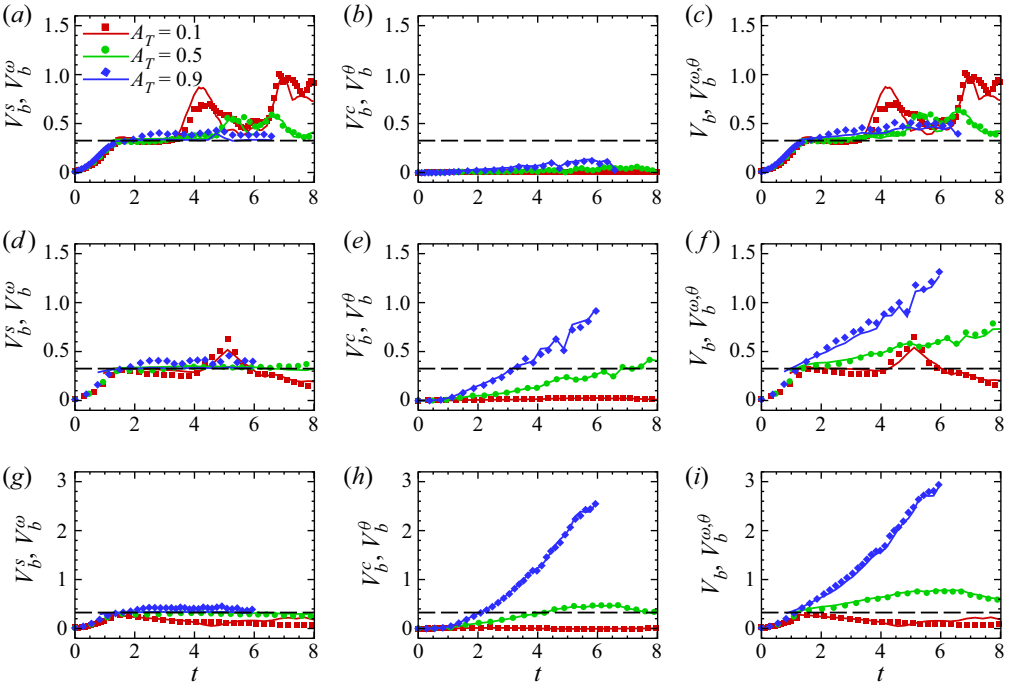

Figure 5. Values of V_b^s, V_b^c and V_b obtained from the DNS (symbols) and V_b^ω, V_b^θ and $V_b^{\omega,\theta}$ calculated by the models (lines) with $Re_p = 10\,000$ versus time for (*a–c*) $Ma = 0.1$, (*d–f*) $Ma = 0.4$ and (*g–i*) $Ma = 0.7$. The horizontal black long dashed line in each panel represents the bubble saturated velocity V_t predicted in potential flow models.

location far away from the bubble tip where the fluid keeps the hydrostatic equilibrium and thus the fluid velocity is zero. Therefore, the upper boundary of the computational domain with the fluid velocity being almost zero is used as $y_{+\infty}$. Considering v^c at the height of the bubble tip is almost uniform along the periodic x-direction and thus can be approximated as V_b^c, the right-hand side of (4.3) is approximated as $-L_x V_b^c$. The left-hand side of (4.3) can be expressed by the spatial average dilatation $\bar{\theta}$ in the region S, i.e. $\iint_S \theta \, \mathrm{d}S = hL_x\bar{\theta}$, where $h = y_{+\infty} - y_b$ is the height of the region S. Thus, V_b^c is modelled as

$$V_b^\theta = -h\bar{\theta}. \tag{4.4}$$

Figure 5(*b*,*e*,*h*) shows excellent agreement between the model prediction (V_b^θ) with the DNS result (V_b^c). Furthermore, for a given A_T, V_b^θ at the RA stage obtains a remarkable increase as Ma is increased, resulting from that the stronger density stratification at higher Ma leads to a greater reduction in drag acting on the bubble and in turn more intense compression of the bubble on the heavy fluid ahead.

By summing the equations (4.2) and (4.4), a novel model describing the bubble RA behaviours in stratified compressible RTI can be obtained as

$$V_b^{\omega,\theta} = \sqrt{\frac{g(1-r_d)}{C_d k} + \eta r_d \frac{\omega_0^2}{4k^2}} - h\bar{\theta}. \tag{4.5}$$

Figure 5(*c*,*f*,*i*) shows that the model (4.5) captures well the bubble velocity development after the potential stage ($t \approx 1.5$). This agreement further supports the interpretation that

both vorticity accumulation inside the bubble tip and flow compressibility are responsible for the bubble RA.

Although our discussion is based on 2-D simulations, the uncovered mechanisms of bubble RA are straightforwardly applicable to the three-dimensional (3-D) compressible RTI, as the model (4.5) can also be extended to the 3-D flows by modelling the V_b^s and V_b^c separately. For 3-D RTI V_b^s can be modelled as the same form of (4.2) in which $C_d = 1$ (Betti & Sanz 2006; Yan *et al.* 2016). On the other hand, V_b^c related to flow compressibility for 3-D situation can be modelled by

$$\iiint_{V'} \theta \,\mathrm{d}V = \oiint_{\partial V'} u^c \,\mathrm{d}y\,\mathrm{d}z + v^c \,\mathrm{d}z\,\mathrm{d}x + w^c \,\mathrm{d}x\,\mathrm{d}y. \tag{4.6}$$

Here, Gauss's law is employed along with the Helmholtz decomposition, $\theta = \partial u_i^c/\partial x_i$, and the gravity direction is fixed along the y-direction. We use V' to denote the integral volume above the bubble tip where the heavy fluid is compressed by the bubble, i.e. $V' = [0, L_x] \times [y_b, y_{+\infty}] \times [0, L_z]$. Considering that v^c at the height of the bubble tip is almost uniform along the periodic x- and z-directions and, thus, can be approximated as V_b^c, the right-hand side of (4.6) is approximated as $-L_x L_z V_b^c$. Similar to the 2-D case, the left-hand side of (4.6) is expressed by the spatially averaged dilatation $\bar{\theta}$ in the volume V', i.e. $\iiint_{V'} \theta \,\mathrm{d}V = hL_xL_z\bar{\theta}$, where $h = y_{+\infty} - y_b$ is the height of the volume V'. Thus, V_b^c is also modelled as $V_b^\theta = -h\bar{\theta}$. To this end, the model $V_b^{\omega,\theta}$ is extended to the 3-D compressible RTI and has the same form as its 2-D counterpart, i.e. (4.5).

To verify that the model $V_b^{\omega,\theta}$ is applicable to the 3-D case, the 3-D stratified compressible RTI for $Re_p = 1500$ has been simulated in three typical cases: (1) $Ma = 0.1$, $A_T = 0.1$ corresponding to the bubble RA determined by vorticity accumulation; (2) $Ma = 0.7$, $A_T = 0.9$ corresponding to the bubble RA dominated by flow compressibility; (3) $Ma = 0.7$, $A_T = 0.1$ corresponding to the bubble deceleration. Here, the computational domain is set as $L_x \times L_y \times L_z = [0, 1] \times [-5, 5] \times [0, 1]$ and the uniform cubic mesh size $\Delta = 0.01$ is used. Considering that the horizontal component of vorticity accelerates the bubble growth (Yan *et al.* 2016), the vorticity term in (4.5) is calculated as $\omega_0 = \int_V \rho\sqrt{\omega_x^2 + \omega_z^2}\,\mathrm{d}V / \int_V \rho\,\mathrm{d}V$ for 3-D cases, where ω_x and ω_z are the x- and z-directions components of vorticity, respectively. The efficiency factor of the vorticity term in (4.5) is selected as $\eta = 0.85$ for 3-D cases. It is clearly seen in figure 6 that V_b^ω and V_b^θ agree well with V_b^s and V_b^c evaluated from the simulations, respectively, and the current model $V_b^{\omega,\theta}$ also captures well the 3-D bubble velocity development after the potential stage ($t \approx 2.0$). This agreement further supports that the two mechanisms accounting for the bubble RA are applicable to the 3-D compressible RTI. To this point, the model $V_b^{\omega,\theta}$ provides a theoretical basis for the systematic study of nonlinear behaviours for 3-D stratified compressible RTI in the future.

5. Concluding remarks

In summary, highly nonlinear bubble evolution occurring in a single-mode stratified compressible RTI has been reported via DNS. Specifically, the bubble RA behaviours are found except in the cases with high Ma quantifying the isothermal stratification and small A_T. For small Ma, both decreasing A_T and increasing Re_p make the bubble RA more intense, which is the same as that in the quasi-incompressible RTI with uniform background density. However, it is interesting that for high Ma, increasing A_T enhances the bubble development and Re_p has little effect on the bubble RA behaviour.

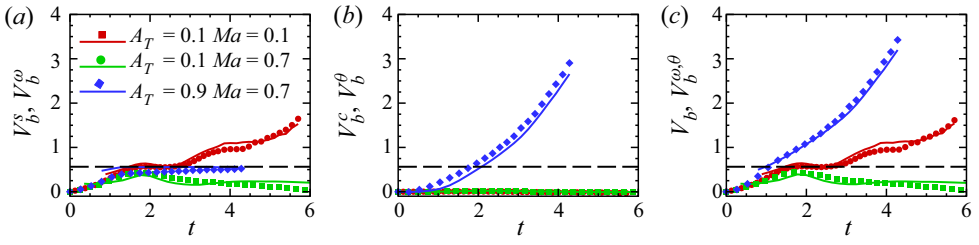

Figure 6. Values of V_b^s, V_b^c and V_b obtained from the simulations (symbols) and V_b^ω, V_b^θ and $V_b^{\omega,\theta}$ calculated by the 3-D models (lines) with $Re_p = 1500$ versus time for three typical cases. The horizontal black long dashed line in each panel represents the 3-D bubble saturated velocity predicted in potential flow models.

This flow phenomenon is ascribed to flow compressibility which results from the background stratification and sets in the bubble RA as a novel mechanism coupled with vorticity accumulation inside the bubble for stratified compressible RTI. Inspired by the aforementioned flow physics, a novel model has been proposed via the introduction of the dilatation to account for the effects of flow compressibility, into the classical RA model that only takes into account vorticity accumulation. This improved model performs reliably to capture the bubble velocity development after the potential stage in the stratified compressible RTI.

Note that the current novel bubble RA model which inherits the illuminating idea of the Betti–Sanz model (Betti & Sanz 2006), still requires the simulation and thus is not predictive. Nevertheless, it succeeds in quantifying the importance of flow compressibility and vorticity accumulation to the bubble growth in stratified compressible RTI, presenting a functional description of bubble velocity. One should keep in mind that, due to the challenging complexity and high nonlinearity of the late-time bubble behaviour in compressible RTI, a predictive model to describe the bubble RA is still lacking. To this point, we believe that the bubble RA mechanism quantified in this extended model would be instructive to the research community working to develop a predictive model for the nonlinear bubble behaviour.

Acknowledgements. The authors are very grateful to Professor R. Yan at USTC for helpful discussions and Dr Y.-S. Zhang at the Institute of Applied Physics and Computational Mathematics for technical support.

Funding. This work was supported by the National Natural Science Foundation of China (Nos. 11621202, 12202436 and 92052301), LCP Fund for Young Scholar (No. 6142A05QN22002) and the Fundamental Research Funds for the Central Universities.

Declaration of interests. The authors report no conflicts of interest.

Author ORCIDs.
Cheng-Quan Fu https://orcid.org/0000-0001-8320-3839;
Zhiye Zhao https://orcid.org/0000-0003-1509-5084;
Nan-Sheng Liu https://orcid.org/0000-0001-9128-1933;
Zhen-Hua Wan https://orcid.org/0000-0003-0035-3116;
Xi-Yun Lu https://orcid.org/0000-0002-0737-6460.

References

Banerjee, R., Mandal, L., Roy, S., Khan, M. & Gupta, M.R. 2011 Combined effect of viscosity and vorticity on single mode Rayleigh–Taylor instability bubble growth. *Phys. Plasmas* **18**, 022109.

BETTI, R. & SANZ, J. 2006 Bubble acceleration in the ablative Rayleigh–Taylor instability. *Phys. Rev. Lett.* **97**, 205002.

BIAN, X., ALUIE, H., ZHAO, D.-X., ZHANG, H. & LIVESCU, D. 2020 Revisiting the late-time growth of single-mode Rayleigh–Taylor instability and the role of vorticity. *Physica* D **403**, 132250.

BURROWS, A. 2000 Supernova explosions in the universe. *Nature* **403**, 727–733.

CABOT, W.H. & COOK, A.W. 2006 Reynolds number effects on Rayleigh–Taylor instability with possible implications for type Ia supernovae. *Nat. Phys.* **2**, 562–568.

FU, C.-Q., ZHAO, Z.-Y., XU, X., WANG, P., LIU, N.-S., WAN, Z.-H. & LU, X.-Y. 2022 Nonlinear saturation of bubble evolution in a two-dimensional single-mode stratified compressible Rayleigh–Taylor instability. *Phys. Rev. Fluids* **7**, 023902.

GONCHAROV, V.N. 2002 Analytical model of nonlinear, single-mode, classical Rayleigh–Taylor instability at arbitrary Atwood numbers. *Phys. Rev. Lett.* **88**, 134502.

HOUSEMAN, G.A. & MOLNAR, P. 1997 Gravitational (Rayleigh–Taylor) instability of a layer with non-linear viscosity and convective thinning of continental lithosphere. *Geophys. J. Intl* **128**, 125–150.

HU, Z.-X., ZHANG, Y.-S. & TIAN, B.-L. 2020 Evolution of Rayleigh–Taylor instability under interface discontinuous acceleration induced by radiation. *Phys. Rev.* E **101**, 043115.

HU, Z.-X., ZHANG, Y.-S., TIAN, B.-L., HE, Z.-W. & LI, L. 2019 Effect of viscosity on two-dimensional single-mode Rayleigh–Taylor instability during and after the reacceleration stage. *Phys. Fluids* **31**, 104108.

LAYZER, D. 1955 On the instability of superposed fluids in a gravitational field. *Astrophys. J.* **122**, 1–12.

LI, H.-F., HE, Z.-W., ZHANG, Y.-S. & TIAN, B.-L. 2019 On the role of rarefaction/compression waves in Richtmyer–Meshkov instability with reshock. *Phys. Fluids* **31**, 054102.

LIVESCU, D. 2004 Compressibility effects on the Rayleigh–Taylor instability growth between immiscible fluids. *Phys. Fluids* **16**, 118–127.

LUO, T.-F. & WANG, J.-C. 2021 Effects of Atwood number and stratification parameter on compressible multi-mode Rayleigh–Taylor instability. *Phys. Fluids* **33**, 115111.

LUO, T.-F., WANG, J.-C., XIE, C.-Y., WAN, M.-P. & CHEN, S.-Y. 2020 Effects of compressibility and Atwood number on the single-mode Rayleigh–Taylor instability. *Phys. Fluids* **32**, 012110.

RAMAPRABHU, P., DIMONTE, G., WOODWARD, P., FRYER, C., ROCKEFELLER, G., MUTHURAMAN, K., LIN, P.H. & JAYARAJ, J. 2012 The late-time dynamics of the single-mode Rayleigh–Taylor instability. *Phys. Fluids* **24**, 074107.

RAMAPRABHU, P., DIMONTE, G., YOUNG, Y.N., CALDER, A.C. & FRYXELL, B. 2006 Limits of the potential flow approach to the single-mode Rayleigh–Taylor problem. *Phys. Rev.* E **74**, 066308.

RAYLEIGH, LORD 1882 Investigation of the character of the equilibrium of an incompressible heavy fluid of variable density. *Proc. R. Math. Soc.* **s1-14**, 170–177.

RECKINGER, S.J., LIVESCU, D. & VASILYEV, O.V. 2012 Simulations of compressible Rayleigh–Taylor instability using the adaptive wavelet collocation method. In *Seventh International Conference on Computational Fluid Dynamics (ICCFD7), Big Island, Hawaii*.

RECKINGER, S.J., LIVESCU, D. & VASILYEV, O.V. 2016 Comprehensive numerical methodology for direct numerical simulations of compressible Rayleigh–Taylor instability. *J. Comput. Phys.* **313**, 181–208.

SWISHER, N.C., KURANZ, C.C., ARNETT, D., HURRICANE, O., REMINGTON, B.A., ROBEY, H.F. & ABARZHI, S.I. 2015 Rayleigh–Taylor mixing in supernova experiments. *Phys. Plasmas* **22**, 102707.

TAYLOR, G.I. 1950 The instability of liquid surfaces when accelerated in a direction perpendicular to their planes. I. *Proc. R. Soc. Lond.* A **201**, 192–196.

WANG, J.C., YANG, Y.T., SHI, Y.P., XIAO, Z.L., HE, X.T. & CHEN, S.Y. 2013 Cascade of kinetic energy in three-dimensional compressible turbulence. *Phys. Rev. Lett.* **110**, 214505.

WEI, T. & LIVESCU, D. 2012 Late-time quadratic growth in single-mode Rayleigh–Taylor instability. *Phys. Rev.* E **86**, 046405.

WIELAND, S.A., HAMLINGTON, P.E., RECKINGER, S.J. & LIVESCU, D. 2019 Effects of isothermal stratification strength on vorticity dynamics for single-mode compressible Rayleigh–Taylor instability. *Phys. Rev. Fluids* **4**, 093905.

WILCOCK, W.S.D. & WHITEHEAD, J.A. 1991 The Rayleigh–Taylor instability of an embedded layer of low-viscosity fluid. *J. Fluid Mech.* **96**, 12193–12200.

WILKINSON, J.P. & JACOBS, J.W. 2007 Experimental study of the single-mode three-dimensional Rayleigh–Taylor instability. *Phys. Fluids* **19**, 124102.

YAN, R., BETTI, R., SANZ, J., ALUIE, H., LIU, B. & FRANK, A. 2016 Three-dimensional single-mode nonlinear ablative Rayleigh–Taylor instability. *Phys. Plasmas* **23**, 022701.

ZHANG, H., BETTI, R., YAN, R. & ALUIE, H. 2020 Nonlinear bubble competition of the multimode ablative Rayleigh–Taylor instability and applications to inertial confinement fusion. *Phys. Plasmas* **27**, 122701.

ZHAO, D.-X., BETTI, R. & ALUIE, H. 2022 Scale interactions and anisotropy in Rayleigh–Taylor turbulence. *J. Fluid Mech.* **930**, A29.

ZHAO, Z.-Y., LIU, N.-S. & LU, X.-Y. 2020*a* Kinetic energy and enstrophy transfer in compressible Rayleigh–Taylor turbulence. *J. Fluid Mech.* **904**, A37.

ZHAO, Z.-Y., WANG, P., LIU, N.-S. & LU, X.-Y. 2020*b* Analytical model of nonlinear evolution of single-mode Rayleigh–Taylor instability in cylindrical geometry. *J. Fluid Mech.* **900**, A24.

ZHAO, Z.-Y., WANG, P., LIU, N.-S. & LU, X.-Y. 2021 Scaling law of mixing layer in cylindrical Rayleigh–Taylor turbulence. *Phys. Rev.* E **104** (5), 055104.

ZHOU, Y. 2017 Rayleigh–Taylor and Richtmyer–Meshkov instability induced flow, turbulence, and mixing. I. *Phys. Rep.* **720**, 1–136.